Synthesis and Structural Characterization of the Pt_2(II,III) Complex $(NBu_4)[(C_6F_5)_2Pt(\mu\text{-}C_6F_5)_2Pt(C_6F_5)_2]$ and the Pt_2(III,III) Complex $(NBu_4)[(C_6F_5)_2Pt(\mu\text{-}C_6F_5Cl)(\mu\text{-}C_6F_5)Pt(C_6F_5)_2]$. Novel Ligand Reactivity of a Bridging C_6F_5 Group

Rafael Usón,* Juan Forniés, Milagros Tomás, Jose M. Casas, F. Albert Cotton,* Larry R. Falvello, and Xuejun Feng

Contribution from the Departamento de Química Inorgánica and Instituto de Ciencia de Materiales de Aragón, Universidad de Zaragoza-C.S.I.C., 50009 Zaragoza, Spain, and Department of Chemistry and Laboratory for Molecular Structure and Bonding, Texas A&M University, College Station, Texas 77843

Received January 11, 1993

Abstract: The previously reported trinuclear, (C_6F_5)-bridged compound $(NBu_4)[Pt_2(\mu\text{-}C_6F_5)_2(\mu\text{-}AgOEt_2)(C_6F_5)_4]$, **1**, reacts with an excess of molecular chlorine in toluene/CCl_4 to give the novel metal–metal bonded, garnet-colored complex **3**, $(NBu_4)[(C_6F_5)_2Pt(\mu\text{-}C_6F_5Cl)(\mu\text{-}C_6F_5)Pt(C_6F_5)_2]$. Compound **3** is the result of addition of one chlorine atom to a bridging C_6F_5 ligand, with concomitant oxidation of the dinuclear core to a singly bonded Pt(III)–Pt(III) unit with planar D_{2h} geometry. Compound **1** also reacts with an excess of Br_2 or I_2 in toluene to give the black, dinuclear Pt(II)–Pt(III) compound $(NBu_4)[(C_6F_5)_2Pt(\mu\text{-}C_6F_5)_2Pt(C_6F_5)_2]$, **4**, which also has a planar core. The garnet complex **3** can also be prepared by the reaction of the dinuclear, (C_6F_5)-bridged complex $(NBu_4)_2[Pt_2(\mu\text{-}C_6F_5)_2(C_6F_5)_4]$, **2**, with Cl_2 in CCl_4, and by the reaction of compound **4** with Cl_2 in CH_2Cl_2/CCl_4. An SCF-Xα-SW study of compound **4** shows that the HOMO, $15b_{1u}$, which contains an unpaired electron, takes its major contribution from the π system of the bridging (C_6F_5) ligands, thus explaining the vulnerability of the bridging ligand to chemical attack. Complex **3** has been characterized by ^{19}F NMR spectroscopy and by X-ray diffraction. Complex **4** was studied by EPR spectroscopy and X-ray diffraction. Compound **3**, $Pt_2C_{52}H_{36}NF_{30}Cl$, crystallizes in the monoclinic crystal system, space group $C2/c$, with a = 12.101(3) Å, b = 21.047(6) Å, c = 21.977(8) Å, β = 95.57(3)°, V = 5571(3) Å^3 at −83 °C, and Z = 4. A model of 353 parameters was refined to residuals of R = 0.0629, R_w = 0.0909, and quality of fit = 1.708. Compound **4**, $Pt_2C_{52}H_{36}NF_{30}$, is monoclinic, space group $C2/c$, with a = 12.198(6) Å, b = 20.592(6) Å, c = 22.223(7) Å, β = 95.23(3)°, V = 5559(6) Å^3 at 21 °C, and Z = 4. The structure was refined to residuals of R = 0.0431, R_w = 0.0498, and quality of fit = 0.998. The Pt–Pt distances are 2.573(2) and 2.611(2) Å in **3** and **4**, respectively. Cyclic voltammetry shows that a reversible one-electron process interconverts complexes **2** and **4**; however, oxidation of complex **4** by a process presumed to involve ligand reactivity is irreversible.

Introduction

We have recently reported[1,2] the synthesis of polynuclear complexes with the stoichiometries $(NBu_4)_2[MM'(C_6F_5)_6]$ (M = M′ = Pd or Pt; M = Pd, M′ = Pt) and $(NBu_4)[Pt_2Ag(C_6F_5)_6OEt_2]$. The structures of two platinum complexes were determined, and they showed that two of the pentafluorophenyl groups act as bridging ligands in $(NBu_4)[Pt_2(\mu\text{-}C_6F_5)_2(\mu\text{-}AgOEt_2)(C_6F_5)_4]$ (**1**) and $(NBu_4)_2[Pt_2(\mu\text{-}C_6F_5)_2(C_6F_5)_4]$ (**2**). Compound **1** also contains an additional bridge (μ-$AgOEt_2$) formed by the silver cation directly bonded to the two platinum atoms. These are the only platinum complexes containing bridging C_6F_5 groups, and a study of their reactivity was undertaken in order to test the stability of the bridging system. The reactivity toward neutral ligands has already been explored.[2] We present in this paper the results of the reactions with halogens, which lead to novel Pt_2(II,III) and Pt_2(III,III) complexes with unprecedented structural features.

Results and Discussion

(a) Reaction of $(NBu_4)[Pt_2(\mu\text{-}C_6F_5)_2(\mu\text{-}AgOEt_2)(C_6F_5)_4]$ (1) with Chlorine. A toluene suspension of the yellow complex **1** reacts with an excess of chlorine (eq 1) to give complex **3** (90% yield) as an air- and moisture-stable garnet solid.

$$(NBu_4)[Pt_2(\mu\text{-}C_6F_5)_2(\mu\text{-}AgOEt_2)(C_6F_5)_4] + Cl_2 \rightarrow \underset{\mathbf{1}}{} OEt_2 + AgCl + (NBu_4)[(C_6F_5)_2Pt(\mu\text{-}C_6F_5Cl)(\mu\text{-}C_6F_5)Pt(C_6F_5)_2] \quad (1)$$
$$\mathbf{3}$$

The formation of the dark garnet Pt(III)–Pt(III) complex **3** via the novel reaction in eq 1 can be seen as the result of heterolytic cleavage of the chlorine molecule with attack by the electrophilic Cl^+ on the para position of one of the bridging C_6F_5 ligands. The negative Cl^- precipitates as AgCl with the silver ion of the starting material. The bridging ligand which suffers the attack by chlorine loses its aromatic character, and both the ligated and para carbon atoms can be considered to be sp^3 hybridized. We assign a formal charge of (−2) to the bridging C_6F_5Cl ligand of product **3**, so that both platinum atoms are in the formal oxidation state III.

Analytical and conductance data for **3** are in agreement with the proposed stoichiometry (Table I). Absorptions typical of the C_6F_5 groups[3] are observed in the infrared spectrum (see Experimental Section), although the presence of the C_6F_5Cl ligand

(1) Usón, R.; Forniés, J.; Tomás, M.; Casas, J. M.; Cotton, F. A.; Falvello, L. R.; Llusar, R. *Organometallics* **1988**, *7*, 2279.
(2) Usón, R.; Forniés, J.; Tomás, M.; Casas, J. M.; Navarro, R. *J. Chem. Soc., Dalton Trans.* **1989**, 169.
(3) Maslowsky, E., Jr. *Vibrational Spectra of Organometallic Compounds*; Wiley: New York, 1977, p 437.

0002-7863/93/1515-4145$04.00/0

Table I. Analytical[a] and Conductivity Data[b]

		C	H	N	Cl	Λ_M, ohm^{-1} cm^2 mol^{-1}
$(NBu_4)[Pt_2(\mu\text{-}C_6F_5)(\mu\text{-}C_6F_5Cl)(C_6F_5)_4]$	**3**	37.18	2.07	0.78	2.60	114
		(37.39)	(2.17)	(0.84)	(2.12)	
$(NBu_4)[Pt_2(\mu\text{-}C_6F_5)_2(C_6F_5)_4]$	**4**[c]	38.18	1.99	1.02		113
	4[d]	38.20	2.03	1.22		
		(38.20)	(2.22)	(0.86)		

[a] Calculated values in parentheses. [b] In acetone, $c \cong 5 \times 10^{-4}$ M. [c] Oxidation with Br_2. [d] Oxidation with I_2.

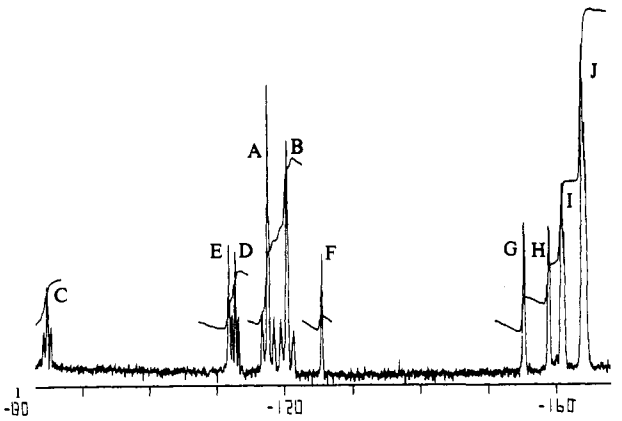

Figure 1. The ^{19}F NMR spectrum of $(NBu_4)[Pt_2(\mu\text{-}C_6F_5)(\mu\text{-}C_6F_5Cl)(C_6F_5)_4]$ (**3**) in $CDCl_3$. The horizontal axis is labeled in ppm.

prevents an unambiguous assignment. The negative ion FAB mass spectrum of the complex ion **3** correctly matches the calculated natural-abundance distribution in the region of the ion peak, at and around 1427 Da.

(i) ^{19}F NMR Spectrum of Complex 3. The spectrum is shown in Figure 1, and its complexity reflects the variety of inequivalences arising from the structure. No less than four multiplets due to the 12 *o*-F atoms are present (labeled A (−117.4 ppm), B (−120.1 ppm), C (−84.5 ppm), and D (−111.6 ppm) in Figure 1). From their relative abundances (A:**B**:C:D = 2:2:1:1) and the relative intensity of the ^{195}Pt satellites, signals A and B are assigned to *o*-F atoms of the four terminal C_6F_5 groups, with the two sets arising from the inequivalence of two terminal groups *trans* to the bridging C_6F_5 and two other terminal groups *trans* to C_6F_5Cl. Signals C and D correspond therefore to the *o*-F atoms of the two different bridging groups.

Each of the two triplets E (−111.6 ppm) and F (−125.2 ppm) is due to only one F atom, as indicated by the two integrated intensities; and we assign the two signals to the *p*-F atoms of the bridging groups. Both signals appear at lower fields and are located at very different chemical shifts from those of the corresponding signals found previously (−153.6 ppm) for *p*-F atoms in bridging C_6F_5 groups in Pt(II) complexes.[2] This deshielding is a consequence of the higher oxidation state of the platinum centers. Moreover, we can tentatively assign signal E to the *p*-F atom of the C_6F_5Cl group, since this atom is expected to be further deshielded by the electrostatic influence of the geminal chlorine atom on the same sp^3-hybridized carbon. Signals G (−155.0 ppm) and H (−158.7 ppm) are assigned to the *m*-F atoms of the bridging groups, and the two remaining multiplets centered at I (−160.7 ppm) and J (−163.7 ppm) are due to the *p*-F and *m*-F atoms, respectively, of the terminal C_6F_5 ligands. A comparison of the present observations with the ^{19}F NMR spectra of complexes **1** and **2** shows that while only small differences appear in the signals of the fluorine atoms of the terminal groups, dramatic changes are observed for the signals arising from the bridging groups.

(ii) Crystal Structure of $(NBu_4)[(C_6F_5)_2Pt(\mu\text{-}C_6F_5Cl)(\mu\text{-}C_6F_5)Pt(C_6F_5)_2]$ (3). General crystallographic information for compound **3** is collected in Table II, and a selection of bond distances and angles is given in Table III. Figure 2 is a drawing of the complex anion, showing the atom naming scheme.

Table II. Crystal Data for Garnet $(NBu_4)[(C_6F_5)_2Pt(\mu\text{-}C_6F_5)(\mu\text{-}C_6F_5Cl)Pt(C_6F_5)_2]$ (**3**) and Black $(NBu_4)[(C_6F_5)_2Pt(\mu\text{-}C_6F_5)_2Pt(C_6F_5)_2]$ (**4**)

	3	**4**
formula	$Pt_2C_{52}H_{36}NF_{30}Cl$	$Pt_2C_{52}H_{36}NF_{30}$
fw	1670.4	1635.0
space group	C2/c	C2/c
systematic absences	(hkl): h + k ≠ 2n; (h01): l (h) ≠ 2n	
a, Å	12.101 (3)	12.198(6)
b, Å	21.047(6)	20.592(6)
c, Å	21.977 (8)	22.223(7)
β, deg	95.57 (3)	95.23(3)
V, Å^3	5571 (3)	5559(6)
Z	4	4
d_{calcd}, g/cm^3	1.991	1.953
cryst size, mm	0.015 × 0.129 × 0.489	0.29 × 0.17 × 0.07
μ(MoKα), cm^{-1}	54.76	54.4
transmission factors: max, min	0.921, 0.536	obsd. 1.00, 0.85
data collecn instrument	Enraf-Nonius CAD-4S	
radiation (graphite monochromated)	Mo Kα ($\lambda_{\bar{a}}$ = 0.71073 Å)	
orientation reflecns:		
no.; range (2θ), deg	24; 21.0–35.0	24; 14–26
temp, °C	−83 ± 1	21.0 ± 0.3
scan method	ω-scan (see text)	ω–2θ
data collecn range, 2θ, deg	4.0–48.0	4.0–50.0
no. of unique data	4329	3426, $F_o^2 \geq 0.3\sigma(F_o^2)$
no. of data with $F_o^2 \geq 3\sigma(F_o^2)$	2447	2532
no. of parameters refined	353	385
R[a]	0.0629	0.0431
R_w[b]	0.0909	0.0498
quality of fit indicator[c]	1.708	0.998
weighting parameter *g*[d]	0.0015	0.0009
largest shift/esd, final cycle	0.08	0.13
largest diff peak, trough, e/Å^3	1.11, −0.91	0.85, −1.10

[a] $R = \sum||F_o|-|F_c||/\sum|F_o|$. [b] $R_w = [\sum w(|F_o|-|F_c|)^2/\sum w|F_o|^2]^{1/2}$. [c] Quality of fit = $[\sum w(|F_o| - |F_c|)^2/(N_{observns} - N_{parameters})]^{1/2}$. [d] $w = [\sigma^2(F_{obs}) + g(F_{obs})^2]^{-1}$.

The determination of the crystal structure of compound **3** presented an unusual assortment of problems, as we describe in detail in the Experimental Section. As Figure 2 shows, the dinuclear compound does not possess a center of inversion; the moieties which deviate from centrosymmetry are the bridging aromatic C_6F_5 and nonaromatic C_6F_5Cl ligands. These ligands are, however, disordered between them; and the anion sits across a crystallographic inversion center. The remaining components of the structure—the unique platinum atom, the terminal C_6F_5 ligands, and the tetrabutylammonium cation (which sits on a crystallographic diad axis)—presented no problems in the development and refinement of the structure. Not only were these entities located and refined straightforwardly, but also the positional parameters of these atoms are nearly identical to the results obtained in routine fashion for the quasi-isostructural $(NBu_4)[(C_6F_5)_2Pt(\mu\text{-}C_6F_5)_2Pt(C_6F_5)_2]$ (**4**)—as a comparison of atomic coordinates from the two structures clearly shows. The presence of a single additional unique atom in the present structure, as compared to compound **4**, leads to disorder, to packing stress,

Table III. Selected Bond Distances and Angles and Their Estimated Standard Deviations for $(NBu_4)[(C_6F_5)_2Pt(\mu\text{-}C_6F_5)(\mu\text{-}C_6F_5Cl)Pt(C_6F_5)_2]$ (**3**)[a]

		Distance, Å	
Pt(1)–Pt(1′)	2.573(2)	Pt(1)–C(1A′)	1.841(22)
Pt(1)–C(1)	2.271(19)	C(7)–C(8)	1.463(28)
Pt(1)–C(1A)	1.962(22)	C(7)–C(12)	1.425(31)
Pt(1)–C(7)	1.964(21)	C(13)–C(14)	1.378(27)
Pt(1)–C(13)	2.011(19)	C(13)–C(18)	1.414(28)
Pt(1)–C(1′)	2.257(20)		
		Angle, deg	
Pt(1′)–Pt(1)–C(1)	55.1(5)	Pt(1′)–Pt(1)–C(1A′)	49.5(7)
Pt(1′)–Pt(1)–C(1A)	45.5(7)	C(7)–Pt(1)–C(1A′)	89.7(9)
Pt(1′)–Pt(1)–C(7)	138.5(6)	C(13)–Pt(1)–C(1A′)	167.7(9)
Pt(1′)–Pt(1)–C(13)	137.4(5)	C(1)–Pt(1′)–C(1A)	105.1(9)
C(1)–Pt(1)–C(1A)	100.6(8)	Pt(1)–C(1)–Pt(1′)	69.2(5)
C(1)–Pt(1)–C(7)	84.2(8)	Pt(1)–C(1A)–Pt(1′)	85.1(9)
C(1)–Pt(1)–C(13)	162.7(7)	Pt(1)–C(7)–C(8)	121.5(15)
C(1A)–Pt(1)–C(7)	170.7(8)	Pt(1)–C(7)–C(12)	129.5(16)
C(1A)–Pt(1)–C(13)	92.8(8)	C(8)–C(7)–C(12)	109.0(19)
C(7)–Pt(1)–C(13)	84.1(8)	Pt(1)–C(13)–C(14)	124.0(14)
Pt(1′)–Pt(1)–C(1′)	55.6(5)	Pt(1)–C(13)–C(18)	122.2(14)
C(7)–Pt(1)–C(1′)	162.5(7)	C(14)–C(13)–C(18)	112.7(19)
C(13)–Pt(1)–C(1′)	83.0(7)		

[a] Primed atoms are related to their unprimed congeners by a center of inversion at ($^1/_4$,$^1/_4$,0). Atoms C(1) and C(1A) are ipso carbon atoms of the partially occupied aromatic and nonaromatic rings, respectively. Atoms C(1) and C(1A) are *not* related to each other by the center of inversion.

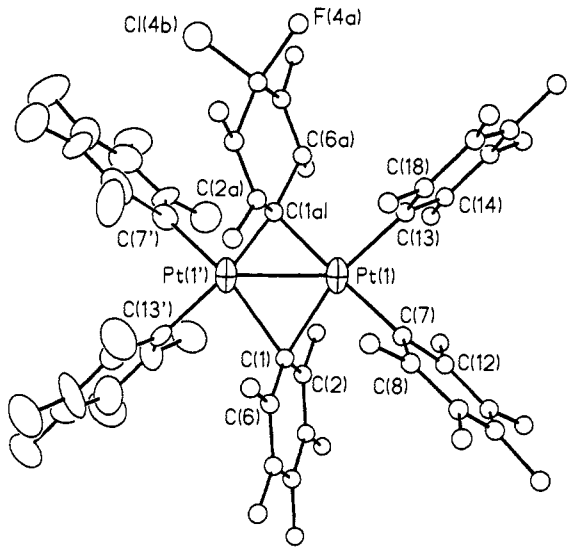

Figure 2. Perspective drawing of the anion $[Pt_2(\mu\text{-}C_6F_5)(\mu\text{-}C_6F_5Cl)(C_6F_5)_4]^-$ from the crystal structure of **3**. Primed atoms are related to their unprimed congeners by a crystallographic inversion center. Carbon atoms are numbered sequentially around the rings, and unlabeled fluorine atoms have the same numbers as do the carbon atoms to which they are attached. The atoms labeled F(4a) and Cl(4b) are composite (F,Cl) sites. The platinum atoms and the atoms of a unique set of terminal ligands are represented by their 30% probability ellipsoids.

and to the concomitant problem that crystals of compound **3** resist growing to more than several microns in thickness.

While we do not attribute great accuracy to the positions of the atoms of the bridging ligands, it is clear that the remainder of the atoms are as well determined as they would be in any routine analysis. The most important features of the structure—the platinum-platinum distance and the overall geometry of the anion—are well established.

Each platinum atom in the dinuclear anion is bonded to four carbon atoms in a square-planar arrangement. The two coordination shells share an edge, thus giving the complex a planar core. The short platinum–platinum distance, 2.573(2) Å, is near the low end of the range of Pt–Pt distances (2.547(1)[4] to 2.695(1)[5,6]

Chart I

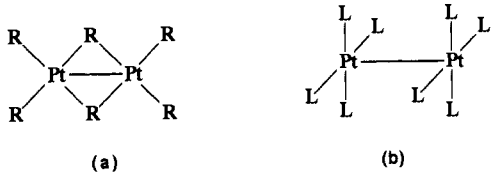

Å) in Pt(III) complexes for which Pt–Pt bonds have been invoked.[7] Since compound **3** is diamagnetic, we conclude that a Pt–Pt bond is present in this complex.

The most striking geometrical feature of compound **3** is the orientation of the Pt–Pt bond with respect to the coordination planes of the two platinum atoms. In this complex all important bonding in the core takes place in one plane, and the core has idealized D_{2h} symmetry (see Chart I, a). This contrasts sharply to the situation in previously reported compounds with Pt–Pt bonds, in which the metal–metal bonds are perpendicular to the ligand coordination planes of the two platinum atoms (Chart I, b), giving these complexes idealized D_{4h} symmetry.

The nature of compound **3**, and especially of its bridging ligands, is well-established by the noncrystallographic data that we have presented. The crystallographic data, while not yielding atomic resolution for most of the individual atoms of the bridging ligands, do indeed establish the presence of out-of-plane substituents at the para position of a bridging ring. The two atomic sites involved, which should correspond to a fluorine and a chlorine atom, were refined free of geometrical restraints or constraints. (Each site was refined as a composite of F and Cl, with the populations constrained so as to maintain a fixed overall stoichiometry.) The two sites refined stably as independent scatterers, outside of the rigid group model used for the rest of the atoms of the bridging ligands.

The diffraction results also do not permit a distinction of the terminal ligands in terms of which one is *trans* to an aromatic bridge. We do not observe any sign (such as extended displacement ellipsoids) that there is a significant difference in the Pt–C distances for the two chemically distinct (but crystallographically equivalent by disorder) types of terminal ligand.

(b) The Reaction of $(NBu_4)[Pt_2(\mu\text{-}C_6F_5)_2(\mu\text{-}AgOEt_2)(C_6F_5)_4]$ (1) with Bromine or Iodine. A toluene suspension of complex **1** reacts with an excess of Br_2 or I_2 to form (eq 2) the black Pt_2(II,III) complex $(NBu_4)[(C_6F_5)_2Pt(\mu\text{-}C_6F_5)_2Pt(C_6F_5)_2]$ (**4**).

$$\underset{\mathbf{1}}{(NBu_4)[Pt_2(\mu\text{-}C_6F_5)_2(\mu\text{-}AgOEt_2)(C_6F_5)_4]} \xrightarrow{Br_2,I_2(\text{excess})} OEt_2 + AgX + \underset{\mathbf{4}}{(NBu_4)[(C_6F_5)_2Pt(\mu\text{-}C_6F_5)_2Pt(C_6F_5)_2]} \quad (2)$$

Yield: X = Br, 41%; X = I, 49%

The black Pt_2(II,III) complex **4** is stable toward air and moisture; and despite the use of an excess of halogen (1:3 mol ratio), the formation of more highly oxidized products has not been detected.

Analytical and conductance data are given in Table I. As for complex **3**, the mass spectrum of **4** in the region of the negative ion peak is identical, within one's ability to compare it, to the distribution calculated from isotope abundances.

(i) Crystal Structure of $(NBu_4)[(C_6F_5)_2Pt(\mu\text{-}C_6F_5)_2Pt(C_6F_5)_2]$ (4). The structure of **4** has been determined by single-crystal

(4) Hollis, L. S.; Roberts, M. M.; Lippard, S. J. *Inorg. Chem.* **1983**, *22*, 3637.
(5) Che, C. M.; Schaefer, W. P.; Gray, H. B.; Dickson, M. K.; Stein, P. B.; Roundhill, D. M. *J. Am. Chem. Soc.* **1982**, *104*, 4253.
(6) Che, C. M.; Herbstein, F. A.; Schaefer, W. P.; Marsh, R. E.; Gray, H. B. *J. Am. Chem. Soc.* **1983**, *105*, 4604.
(7) Woollins, J. D.; Kelly, P. E. *Coord. Chem. Rev.* **1985**, *65*, 115.

Table IV. Selected Bond Distances and Angles and Their Estimated Standard Deviations for $(NBu_4)[(C_6F_5)_2Pt(\mu\text{-}C_6F_5)_2Pt(C_6F_5)_2]$ (4)[a]

	Distance, Å		
Pt(1)–Pt(1′)	2.611(2)	C(1)–C(6)	1.424(21)
Pt(1)–C(1)	2.126(14)	C(7)–C(8)	1.377(20)
Pt(1)–C(1′)	2.148(14)	C(7)–C(12)	1.361(23)
Pt(1)–C(7)	2.043(13)	C(13)–C(14)	1.421(21)
Pt(1)–C(13)	2.004(14)	C(13)–C(18)	1.375(19)
C(1)–C(2)	1.393(22)		
	Angle, deg		
Pt(1′)–Pt(1)–C(1)	52.7(4)	Pt(1)–C(1)–C(2)	113.6(11)
Pt(1′)–Pt(1)–C(1′)	52.0(4)	Pt(1)–C(1)–C(6)	119.3(10)
Pt(1′)–Pt(1)–C(7)	138.7(4)	Pt(1′)–C(1)–C(2)	113.3(10)
Pt(1′)–Pt(1)–C(13)	138.7(4)	Pt(1′)–C(1)–C(6)	117.1(11)
C(1)–Pt(1)–C(1′)	104.7(4)	C(2)–C(1)–C(6)	113.2(13)
C(1)–Pt(1)–C(7)	86.8(5)	Pt(1)–C(7)–C(8)	120.1(11)
C(1)–Pt(1)–C(13)	164.8(6)	Pt(1)–C(7)–C(12)	122.5(11)
C(1′)–Pt(1)–C(7)	165.6(5)	C(8)–C(7)–C(12)	117.4(13)
C(1′)–Pt(1)–C(13)	87.6(5)	Pt(1)–C(13)–C(14)	123.2(10)
C(7)–Pt(1)–C(13)	82.6(5)	Pt(1)–C(13)–C(18)	124.0(11)
Pt(1)–C(1)–Pt(1′)	75.3(4)	C(14)–C(13)–C(18)	112.8(13)

[a] Primed atoms are related to their unprimed congeners by a center of inversion at (1/4,1/4,0).

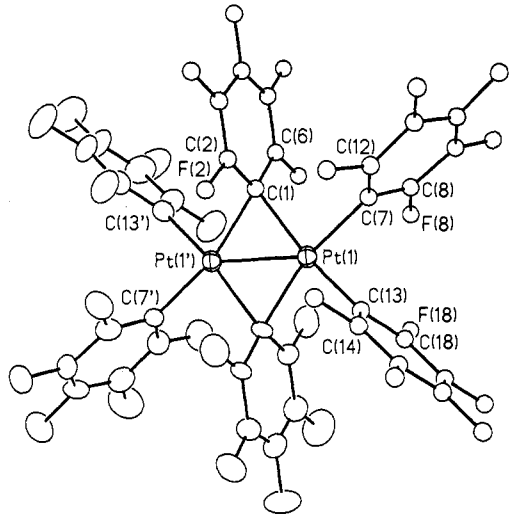

Figure 3. Perspective drawing of the anion $[Pt_2(\mu\text{-}C_6F_5)_2(C_6F_5)_4]^-$ from the crystal structure of 4, with the atom labeling scheme indicated. Carbon and fluorine atoms are numbered sequentially around the C_6F_5 rings. Primed atoms are related to the corresponding unprimed atoms by a crystallographic inversion center. The platinum atoms and a unique set of C and F atoms are represented by their 30% probability ellipsoids.

X-ray diffraction. General crystallographic information is collected in Table II. Selected bond distances and angles are given in Table IV. The structure of the anion in 4 is shown in Figure 3. The entire anion is centrosymmetric, and thus the two platinum atoms are in identical environments and should be assigned an average oxidation state of (+2.5) rather than separate II and III states. Each platinum center is bonded to two terminal and two bridging C_6F_5 groups so as to have slightly distorted square-planar coordination. The Pt–C(7) and Pt–C(13) terminal distances, 2.043(13) and 2.004(14) Å are in the usual range for pentafluorophenyl complexes,[1] and they are shorter than the Pt–C_6F_5 bridging distances of 2.126(14) and 2.148(14) Å, as previously found for $(NBu_4)_2[Pt_2(\mu\text{-}C_6F_5)_2(C_6F_5)_4]\cdot H_2O$ and $(NBu_4)[Pt_2(\mu\text{-}AgOEt_2)(\mu\text{-}C_6F_5)_2(C_6F_5)_4]$.[1] The bond angles around each platinum center are in the range 82.6(5)–104.7(4)°. The "$Pt_2(\mu\text{-}C)_2$" fragment is rigorously planar (as required by the inversion center), and the bridging C_6F_5 groups lie almost perpendicular to the central plane; the dihedral angle is 88.4°, while the angles formed by the "$Pt_2(\mu\text{-}C)_2$" plane with the terminal C_6F_5 groups are 98.8° and 99.1°. The distance between the two platinum atoms, 2.611(2) Å, is shorter than the Pt–Pt distance in the dianionic compound $(NBu_4)_2[Pt_2(\mu\text{-}C_6F_5)_2(C_6F_5)_4]$ (2) (2.714(1) Å),[1] and this fact can be explained by the theoretical study which is discussed below. The Pt–Pt distance in 4 is also shorter than the Pt–Pt distances found either in polynuclear complexes with platinum atoms in the average oxidation state (2.5) (e.g. 2.677(2) Å in $[Pt_2(CH_3CS_2)_4I]$,[8] 2.793(1) Å in $K_4[Pt_2(pop)_4Br]\cdot 3H_2O$,[6] and 2.702(6), 2.710(5), 2.706(6) Å in $[Pt_4(NH_3)_8(C_4H_6NO)_4](NO_3)_6\cdot 2H_2O$[9]) or in binuclear Pt(III) complexes (e.g. 2.695(1) Å in $K_4[Pt_2(pop)_4Cl_2]$[6]) for which Pt–Pt bonds have been postulated. Nevertheless, the Pt–Pt distance in 4 is longer than the Pt–Pt distance in compound 3, for which we have concluded that a Pt–Pt bond of order 1 is present.

It is again remarkable that, as for 3, compound 4 presents a substantially different structure from those of other polynuclear platinum complexes with mixed oxidation state, since for 4 the square-planar environments around each platinum atom are in the same plane while for other complexes the square-planar environments are almost parallel (see Chart I, a and b).

(ii) EPR Spectrum of Complex 4. The X-band EPR spectrum of a powdered sample was taken at liquid N_2 temperature using a VARIAN E-112 spectrometer. The spectrum shows an anisotropic signal with $g_x = 2.16$, $g_y = 2.10$ and $g_z = 1.93$, reminiscent of the EPR spectra of a mononuclear Pt(III) complex prepared from $[PtL_2](PF_6)_2$ (L = 1,4,7-trithiacyclononane)[10] and polynuclear Pt(III)-containing complexes $[Pt_4(NH_3)_8(C_5H_5N_2O_2)_4](NO_3)_5\cdot 5H_2O$;[11] no ^{195}Pt hyperfine coupling interactions are observed.

(c) SCF-Xα Molecular Orbital Study of $[Pt_2(\mu\text{-}C_6F_5)_2(C_6F_5)_4]^-$ (4). SCF-Xα-SW calculations[12] were carried out on a model molecule $[Pt_2(\mu\text{-}C_6F_5)_2(CF_3)_4]^-$ in which the terminal C_6F_5 ligands in the real compound were replaced by CF_3 groups. This was necessary to make the project computationally feasible. Based on considerations of electronegativity and the assumption that the terminal ligands are bonded to the metal atoms mainly through the σ bonding interaction of the terminal C atoms with the metal, the absence of the π systems of the terminal C_6F_5 groups was considered to be an acceptable approximation.

The atomic coordinates of the Pt atoms, the atoms in the bridging ligands, and the terminal C atoms were idealized by averaging chemically equivalent bond distances and angles from the crystal structure of the real compound. The coordinates of the F atoms in the terminal CF_3 groups were obtained, however, by using the following distance and angle: C–F = 1.335 Å and C–F–C = 105°. The molecule was placed in a coordinate system with its origin at the midpoint of the Pt–Pt axis, which is colinear with the Z axis; the XZ plane was chosen to contain the two μ-C atoms and the four terminal C atoms, and the XY plane to contain the μ-C_6F_5 ligands. The molecule was assumed to possess D_{2h} symmetry, for which the classification of the metal atomic orbitals is given in Table V.

Table V. Splitting of Atomic Orbitals of the Metal Atoms of $[(CF_3)_2Pt(\mu\text{-}C_6F_5)_2Pt(CF_3)_2]^-$ under D_{2h} Symmetry

orbitals	D_{2h} symmetry
d_{z^2}, s, p_z	a_g, b_{1u}
$d_{x^2-y^2}$	a_g, b_{1u}
d_{xy}	b_{1g}, a_u
d_{xz}, p_x	b_{2g}, b_{3u}
d_{yz}, p_y	b_{3g}, b_{2u}

(8) Bellitto, C.; Flamini, A.; Gastaldi, L.; Scaramuzza, L. *Inorg. Chem.* **1983**, *22*, 444.
(9) Matsumoko, K.; Takahashi, H.; Fuwa, K. *Inorg. Chem.* **1983**, *22*, 4086.
(10) Blake, A. J.; Gould, R. O.; Holder, A. J.; Hyde, T. I.; Lavery, A. J.; Odulate, M. O.; Schröder, M. *J. Chem. Soc., Chem. Commun.* **1987**, 118.
(11) Maskarak, P. K.; Williams, I. D.; Lippard, S. J. *J. Am. Chem. Soc.* **1984**, *106*, 6428.
(12) (a) Slater, J. C. *Quatum Theory of Molecules and Solids*; McGraw-Hill: New York, 1974; Vol. IV. (b) Johnson, K. H. *Adv. Quantum Chem.* **1973**, *7*, 143.

Table VI. Upper Valence Molecular Orbitals of $[(CF_3)_2Pt(\mu\text{-}C_6F_5)_2Pt(CF_3)_2]^-$ by Relativistic Calculation

		% contributions						Pt		
level	energy, eV	Pt	C[a]	C[b]	F[b]	C[c]	F[c]	angular contributions		
$15b_{1u}$	−8.983	35	19	36	7	2	1		2% p	98% d
$9a_u$	−9.493	0	0	79	20	0	1			
$9b_{2g}$	−9.504	0	0	79	20	0	1			
$13b_{3g}$	−10.525	8	21	44	16	5	6			
$14b_{1u}$	−11.301	18	1	53	27	0	1	4% s	1% p	95% d
$22a_g$	−11.400	49	3	1	1	23	23	36% s	24% p	40% d
$13b_{1u}$	−11.425	79	0	0	0	9	11	34% s	3% p	63% d
$8b_{2g}$	−11.605	97	0	0	0	0	3			100% d
$20b_{2u}$	−11.890	26	19	5	2	24	24		73% p	27% d
$12b_{3g}$	−12.023	8	18	31	25	5	13			
$8a_u$	−12.280	98	0	0	1	0	1			100% d
$16b_{1g}$	−12.331	96	1	2	0	0	1			100% d
$21a_g$	−12.476	69	8	1	1	11	9	8% s	13% p	79% d
$12b_{1u}$	−12.650	54	9	5	7	12	13		11% p	89% d
$16b_{3u}$	−12.961	96	0	1	0	0	3			100% d
$20a_g$	−13.266	85	5	3	3	0	4			100% d
$11b_{1u}$	−14.105	46	13	1	6	5	29	17% s		83% d
$11b_{3g}$ —[d]	−14.278	47	9	0	7	9	28			100% d
$16b_{2u}$ —[d]	−16.705	29	24	8	7	0	32		16% p	84% d
$15a_g$ —[d]	−17.382	38	21	9	6	0	26	32% s	28% p	40% d
$5b_{3g}$	−18.856	13	0	0	0	22	65		24% p	76% d
$14b_{2u}$	−19.076	20	2	8	8	18	44		4% p	96% d
$14a_g$	−19.506	9	1	19	23	12	36	54% s	11% p	35% d
$5b_{1u}$	−19.637	15	2	1	0	21	61	55% s	19% p	26% d

[a] μ-C atoms of C_6F_5 ligands. [b] Atoms, other than μ-C atoms, of C_6F_5 ligands. [c] Atoms of terminal CF_3 ligands. [d] Ligand-based molecular orbitals which are not listed.

The initial molecular potential was a superposition of Herman–Skillman atomic potentials.[13] It was constructed from atomic potentials of Pt(+2.5), F(−0.14), and C(−0.05) of the C_6F_5 groups and F(−0.3) and C(−0.1) of the CF_3 groups. Overlapping atomic sphere radii were taken to be 89% of the atomic number radii.[14] The radius of the outer sphere was chosen to touch the outermost atomic spheres. The partial wave basis consisted of s-, p-, and d-type spherical harmonics on the Pt atoms, s and p on the C and F atoms, and up to $l = 4$ on the outer spheres. The SCF calculation was first carried out nonrelativistically and converged. The relativistic valence and core corrections[15] to the platinum atomic potential were then included, and the calculation reconverged. Watson spheres[16] with charge of +1 and with the same radii as the outer spheres were used to stabilize the energy levels for the anionic complex.

The results of the relativistic SCF-Xα-SW calculation on $[Pt_2(\mu\text{-}C_6F_5)_2(CF_3)_4]^-$ are presented in Table VI. These include the higher-lying occupied valence molecular orbitals and some lower-lying orbitals involved in M–L bonding, but omit most of the total of 120 occupied valence MOs. The MOs which are not shown are all ligand-based and represent the C–C and C–F σ bonds and the F lone pairs. The HOMO ($15b_{1u}$) contains the unpaired electron, and the calculated LUMO-HOMO energy gap is 2.367 eV. The $15b_{1u}$ orbital has its major contribution from a π orbital of the μ-C_6F_5 groups, but it also possesses antibonding character in both Pt–Pt and Pt–(μ-C) senses, as will be discussed later. Just below the HOMO are the $9a_u$ and $9b_{2g}$ orbitals which are predominantly π orbitals of the μ-C_6F_5 ligands which do not interact directly with the metal dimer at all. Thus, for the real molecule, $[Pt_2(\mu\text{-}C_6F_5)_2(C_6F_5)_4]^-$, the π orbitals of the terminal C_6F_5 groups would be expected in an energy range close to that of the $9a_u$ and $9b_{2g}$ orbitals or lower; and a HOMO with similar character to the $15b_{1u}$ orbital would also be expected.

Before turning to a detailed discussion of the results in Table VI, it will be helpful to employ simple group-theoretical analysis to determine the symmetries of the ligand orbitals which can interact directly with the metal dimer. There are two sp^2-hybridized orbitals of a_g and b_{2u} symmetries on the μ-C atoms which point toward the center of the metal dimer. There are also two b_{3g} and two b_{1u} symmetry π orbitals of the μ-C_6F_5 ligands which may interact with the metal dimer through the μ-C atoms. For the terminal CF_3 ligands, it can be shown that the orbitals which have σ interaction with the metal belong to a_g, b_{3g}, b_{1u}, and b_{2u} symmetries.

Let us now consider M–M interaction in $[Pt_2(\mu\text{-}C_6F_5)_2(CF_3)_4]^-$. From Table V and the above analysis it is expected that linear combinations of the d_{xy} or d_{xz} orbitals of the metal atoms would not interact with any ligand orbitals. We should have, therefore, MOs of b_{1g}, a_u, b_{3u}, and b_{2g} symmetries in the MO diagram which are predominantly the M–M δ, δ^*, π, and π^* orbitals. This is exactly the case as shown clearly in Table VI, where the $16b_{1g}$, $8a_u$, $16b_{3u}$, and $8b_{2g}$ orbitals are the ones concerned. Since all of these MOs are fully occupied, they do not make any net contributions to the formation of M–M π and δ bonds. The other components of the π and π^* orbitals are the linear combinations of the d_{yz} orbitals belonging to b_{2u} and b_{3g} symmetries, respectively. These M–M π and π^* orbitals with their maximum distributions pointing directly to the μ-C and terminal C atoms interact strongly with the ligands and, therefore, are involved mostly in forming M–L σ bonds. Such M–L bonding character is mainly distributed in the $14b_{2u}$, $16b_{2u}$, $5b_{3g}$, and $11b_{3g}$ orbitals in Table VI, and will be discussed later. Here we only want to point out that they are not relevant in the discussion of the M–M bonding. The $20b_{2u}$ orbital also has appreciable metal character contributed largely by the metal 6p orbitals. However, this orbital makes an additional contribution to the M–L bonding and is nonbonding in the sense of M–M interaction.

The M–M interaction represented by the MOs of a_g and b_{1u} symmetries is not as clear as in the cases just discussed. It is evident in Table V that both d_{z^2} and $d_{x^2-y^2}$ orbitals of the metal

(13) Herman, F.; Skillman, S. *Atomic Structure Calculations*; Prentice-Hall: Englewood Cliffs, NJ, 1963.
(14) Norman, J. G., Jr. *Mol. Phys.* **1976**, *31*, 1191.
(15) Wood, J. H.; Boring, M. A. *Phys. Rev. B* **1978**, *18*, 2701.
(16) Watson, R. E. *Phys. Rev.* **1958**, *111*, 1108.

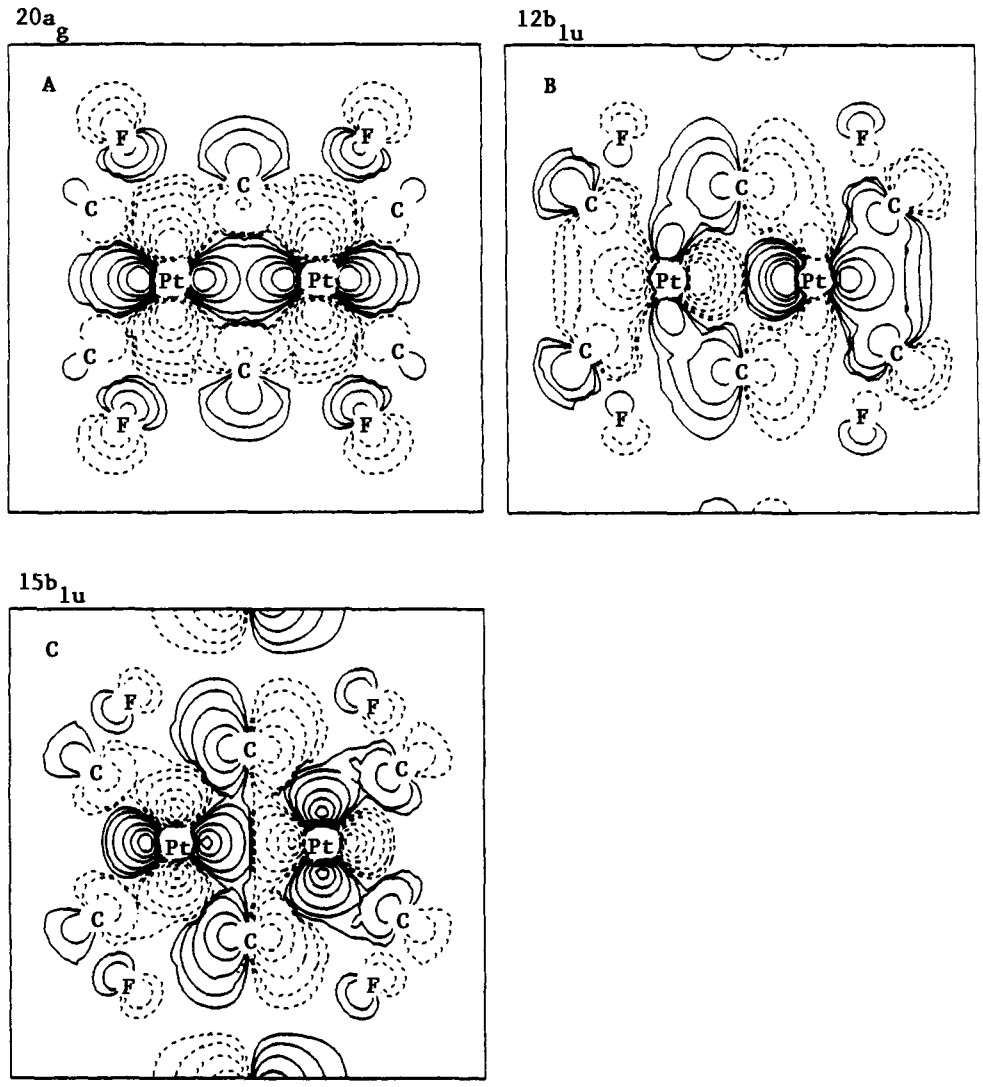

Figure 4. Contour plots of the $20a_g$, $12b_{1u}$, and $15b_{1u}$ orbitals of $[Pt_2(\mu\text{-}C_6F_5)_2(CF_3)_4]^-$. The solid and broken contour lines represent the positive and negative regions, respectively, of the wave function.

atoms span the a_g and b_{1u} representations of the D_{2h} symmetry of the molecule. Thus, the metal contribution to the a_g and b_{1u} MOs is expected to be a combination of hybridized metal AOs. In addition, as can be seen in Table VI, the metal orbitals with significant admixture of s and p characters interact extensively with ligand orbitals of the same symmetries.

There are two a_g and three b_{1u} orbitals which must be considered in discussing the M–M σ and σ^* interactions. These are the $20a_g$, $22a_g$, $12b_{1u}$, $14b_{1u}$, and $15b_{1u}$ orbitals. The $20a_g$ orbital, as its contour plot (Figure 4A) shows, has major M–M σ bonding character. It can be best regarded as composed of overlapping d_{z^2}–$d_{x^2-y^2}$ hybrids, so that the orbital consists of a $d_{z^2-y^2}$–$d_{z^2-y^2}$ combination. The antibonding counterpart of the $20a_g$ orbital is found in both the $12b_{1u}$ and $15b_{1u}$ orbitals (Figure 4, B and C), which have 54% and 35% contributions, respectively, from the metal atoms. The $12b_{1u}$ orbital is also significantly involved in M–L bonding, and the $15b_{1u}$ orbital is only singly occupied. Thus, after cancellation of the σ bonding and antibonding effects, there may still be a σ bond of approximately one-half order left. Very little net bonding can be expected from the $22a_g$ and $14b_{1u}$ orbitals. The $22a_g$ orbital has more metal contribution than the $14b_{1u}$ orbital, but it is mainly an orbital representing bonding between the metal and the terminal C atoms. Its contribution to the M–M bonding is small and is cancelled almost completely by the antibonding effects in the $14b_{1u}$ orbital.

Table VI shows that the $21a_g$ and $13b_{1u}$ orbitals both have dominant metal character. These two orbitals arise mainly from overlap of the $d_{z^2-x^2}$ hybrids supplemented by some s and p overlap. They are effectively δ- and δ^*-type orbitals, as shown by the contours in Figure 5. The orbitals of a_g and b_{1u} symmetries below the $20a_g$ orbital can all be best described as M–L bonding, and therefore can be expected to provide no significant M–M bonding effects.

The bonding of the metal atoms to the terminal ligands is straightforward. The four MOs at the bottom of Table VI are mainly responsible for the bonding of this type. In addition, the $11b_{3g}$, $12b_{1u}$, $20b_{2u}$, and $22a_g$ orbitals also make some contribution to such bonding. Our discussion of the M–L bonding will therefore focus only on that between the metal atoms and the bridging ligands. The presence of C_6F_5 groups as bridging ligands has been observed only in the complexes discussed in this paper and in refs 1 and 2 and is thus very noteworthy because of its novelty.

The interaction of the metal atoms with the μ-C_6F_5 ligands has a dual nature. First, the two sp^2-type orbitals of the μ-C atoms, with a_g and b_{2u} symmetries, are oriented toward the center of the metal dimer and have good overlap with the σ and π orbitals of the dimer. This interaction gives rise to two strongly bonding Pt–(μ-C) orbitals in Table VI, namely the $15a_g$ and $16b_{2u}$ orbitals. These MOs have fairly low energy, and their contour plots are shown in Figure 6. The other type of Pt–(μ-C_6F_5) bonding interaction arises from the overlap of the b_{1u} and b_{3g} orbitals of the metal dimer with certain π orbitals of the bridging ligands having corresponding symmetry, also through the μ-C atoms. This overlap has a form similar to the Pt–(μ-C) bonding character

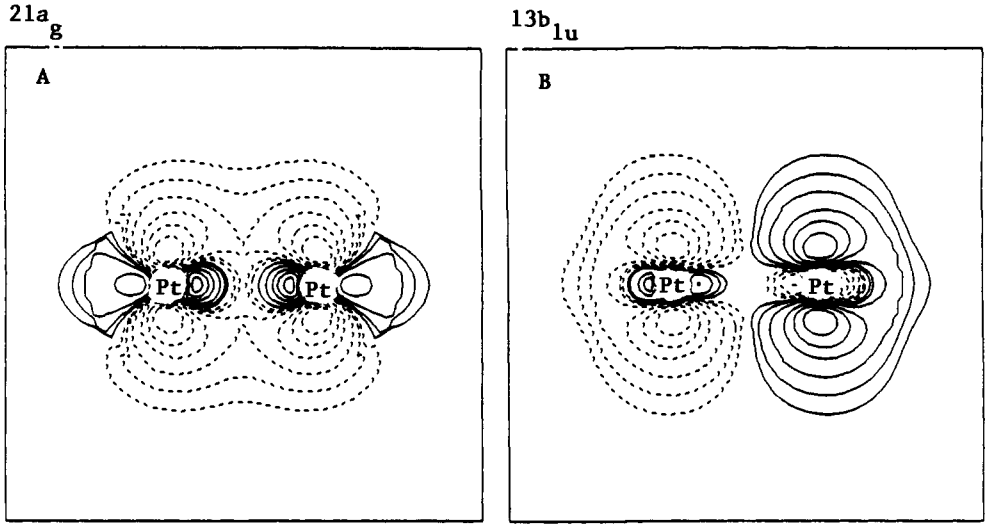

Figure 5. Contour plots of the $21a_g$ and $13b_{1u}$ orbitals of $[Pt_2(\mu\text{-}C_6F_5)_2(CF_3)_4]^-$.

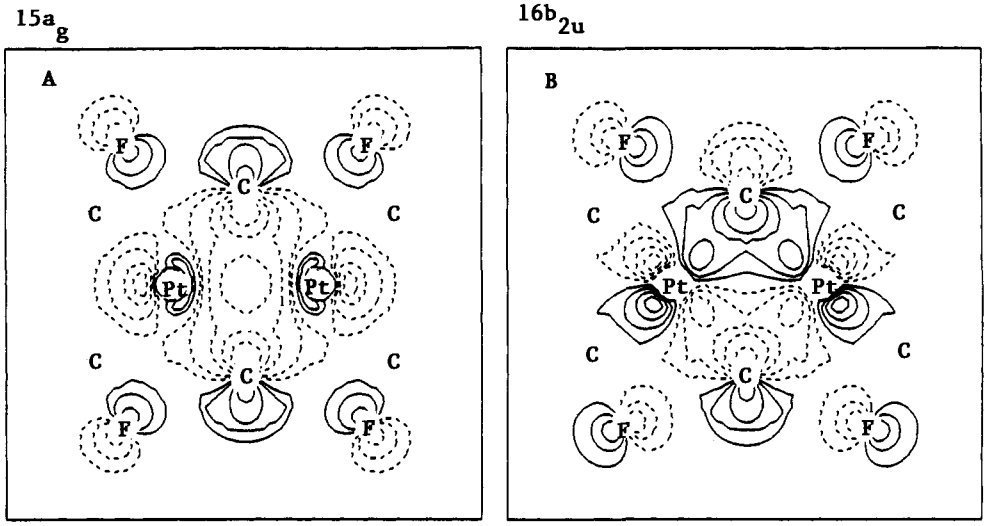

Figure 6. Contour plots of the $15a_g$ and $16b_{2u}$ orbitals of $[Pt_2(\mu\text{-}C_6F_5)_2(CF_3)_4]^-$.

in Figure 4B for the $12b_{1u}$ orbital. In addition to the $12b_{1u}$ orbital contribution, this type of bonding is enhanced by the $11b_{1u}$ and $11b_{3g}$ orbitals. In summation, it may be said that the strong bonding interaction of the metal dimer with the bridging ligands has the effect of pulling the metal atoms toward each other and thus contributes, along with the direct Pt–Pt bonding interaction, to the relatively short Pt–Pt distance. While the participation of the metal 6s and 6p orbitals in the bonding of the molecule is very important, none of these orbitals contributes importantly to the M–M bonding. Their main role is to enhance the metal–ligand bonds.

While the calculation on the $[Pt_2(\mu\text{-}C_6F_5)_2(C_6F_5)_4]^-$ ion has fulfilled our hope of obtaining some insight into the bonding in this species, it does not give as much insight into its chemistry as we would like to have. Because the HOMO, the $15b_{1u}$ orbital, is antibonding in both Pt–Pt and Pt–(μ-C) senses (as can be seen in Figure 4C), we are not surprised to find that the addition of another electron, to give the $[Pt_2(\mu\text{-}C_6F_5)_2(C_6F_5)_4]^{2-}$ ion, **2**, leads to longer (by 0.1 Å) Pt–Pt distances.[1] Beyond this, however, there are important but unanswered questions. One of these is why the (2–) ion is bent whereas the (1–) ion is flat. Another is why (as discussed below) does the (1–) ion fail to undergo a simple, reversible oxidation to the neutral, Pt(III)–Pt(III) molecule, $[Pt_2(\mu\text{-}C_6F_5)_2(C_6F_5)_4]$. Electrochemically, oxidation occurs but is clearly irreversible. Chemically, e.g., with Cl_2, there is attack on a bridging ligand rather than simple removal of one electron.

The computational results may suggest a partial answer to the second question, since the odd electron is appreciably delocalized on the rings of the bridging C_6F_5 groups. Thus, a Cl^+ might naturally attack this part of the molecule, but clearly this idea alone cannot be said to account for the formation of the $C_6F_5Cl^{2-}$ group in the product. From a practical point of view, further lengthy computations did not seem promising enough to be worthwhile.

(d) Reactivity of Complex 4. As we have seen from the SCF-Xα-SW molecular orbital study for complex **4**, the $15b_{1u}$ orbital is singly occupied and antibonding; therefore, complex **4** should be easily oxidized to give a neutral Pt_2(III,III) complex. If the Ag^+ cation were a strong enough oxidizing agent, the following reaction (eq 3) might well proceed. However, the reaction of **4**

$$(NBu_4)[Pt_2(\mu\text{-}C_6F_5)_2(C_6F_5)_4] + AgClO_4 \rightarrow \underset{\mathbf{4}}{} NBu_4ClO_4 + Ag^\circ + [Pt_2(\mu\text{-}C_6F_5)_2(C_6F_5)_4] \quad (3)$$

with $AgClO_4$ does not occur as represented (eq 3). A metallic mirror is formed, as expected. However, it does not consist of metallic silver since it is not soluble in HNO_3, but of platinum since it is soluble in HNO_3 + 3 HCl. From the filtrate complex **1**, $(NBu_4)[Pt_2(\mu\text{-}C_6F_5)_2(\mu\text{-}AgOEt_2)(C_6F_5)_4]$, was recovered (41% yield).

Complex **4** can be oxidized with molecular chlorine to afford complex **3** (50% yield); i.e., an oxidation process takes place but

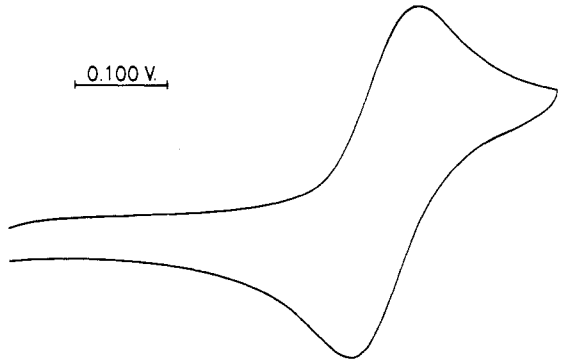

Figure 7. The cyclic voltammogram, at 100 mV·s^{-1} of $(NBu_4)_2[Pt_2(\mu\text{-}C_6F_5)_2(C_6F_5)_4]$ (2) in CH_2Cl_2. $(NBu_4)(PF_6)$ was used as base electrolyte.

a more complicated one than expected, since it includes an attack on one C_6F_5 ring.

Moreover, complex **4** reacts with $(NBu_4)_2[Pt(C_6Cl_5)_4]$ (eq 4), *accepting* one electron to form the yellow $(NBu_4)_2[Pt_2(\mu\text{-}C_6F_5)_2(C_6F_5)_4]$ (**2**) and also producing the previously reported[17] blue monomeric Pt(III) complex $(NBu_4)[Pt(C_6Cl_5)_4]$.

$$\underset{4}{(NBu_4)[Pt_2(\mu\text{-}C_6F_5)_2(C_6F_5)_4]} + (NBu_4)_2[Pt(C_6Cl_5)_4] \rightarrow \underset{2}{(NBu_4)_2[Pt_2(\mu\text{-}C_6F_5)_2(C_6F_5)_4]} + (NBu_4)[Pt(C_6Cl_5)_4] \quad (4)$$

Other attempts to oxidize complex **4** using benzoyl peroxide gave mixtures of unidentified decomposition products.

(e) Reaction of $(NBu_4)_2[Pt_2(\mu\text{-}C_6F_5)_2(C_6F_5)_4]$ (2) with Halogens. The yellow binuclear $Pt_2(II,II)$ complex **2** reacts with Br_2 or I_2 in a THF/toluene solution to give $(NBu_4)_2[Pt_2(\mu\text{-}X)_2(C_6F_5)_4]$ (X = Br (60%), I (73% yield)). If a toluene suspension of **2** is used, the same reaction products are obtained, albeit in lower yields (X = Br, 11%; X = I, 15%) after the same reaction time (60 min), the rest of the product being unreacted starting material (eq 5).

$$\underset{2}{(NBu_4)_2[Pt_2(\mu\text{-}C_6F_5)_2(C_6F_5)_4]} + 2X_2 \rightarrow 2XC_6F_5 + (NBu_4)_2[Pt_2(\mu\text{-}X)_2(C_6F_5)_4] \quad (5)$$

Complex **2** undergoes oxidation with chlorine to afford the dark garnet complex **3**, albeit in lower yield (50%) than is achieved by starting from complex **1**.

(f) Electrochemical Behavior of Complexes 3 and 4. Although in principle the two complexes **2** and **4** are interrelated by a one-electron process (eq 6), we have obtained no evidence supporting

$$\underset{\text{(yellow 2)}}{(NBu_4)_2[Pt_2(\mu\text{-}C_6F_5)_2(C_6F_5)_4]} \overset{-e^-}{\underset{+e^-}{\leftrightarrow}} \underset{\text{(black 4)}}{(NBu_4)[Pt_2(\mu\text{-}C_6F_5)_2(C_6F_5)_4]} \quad (6)$$

this relationship from the reactions of complex **2** with halogens. Nevertheless, complex **2** can be electrochemically oxidized to complex **4**. By applying an increasing voltage (0.45–1.04 V) to a solution of **2** in CH_2Cl_2 (0.10 V·s^{-1}) an oxidation wave was observed at 0.888 V and the reduction peak was at 0.818 V (see Figure 7). The value of $[E_p(ox) - E_p(red)]$ is 0.070 V, showing that it is a one-electron process. As expected, when a decreasing voltage (1.20–0.45 V) is applied, a CH_2Cl_2 solution of **4** shows a reduction wave identical to the oxidation wave of the CH_2Cl_2 solution of **2**, indicating unequivocally that **2** and **4** are the reduced

(17) Usón, R.; Forniés, J.; Tomás, M.; Menjón, B.; Bau, R.; Sünkel, K.; Kuwabara, E. *Organometallics* **1986**, *5*, 1576.

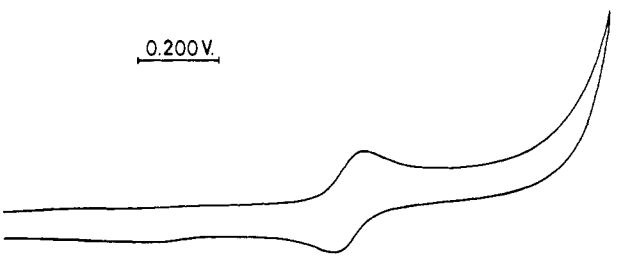

Figure 8. Electrochemical waves from 0 to 2 V of $(NBu_4)[Pt_2(\mu\text{-}C_6F_5)_2(C_6F_5)_4]$ (**4**) in CH_2Cl_2.

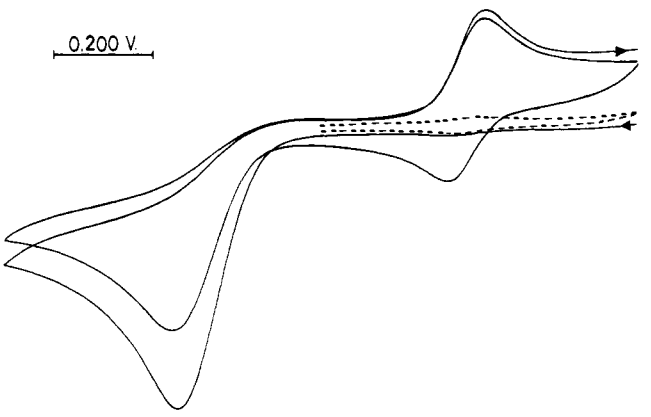

Figure 9. Electrochemical waves from 1.200 to –0.090 V for $(NBu_4)[Pt_2(\mu\text{-}C_6F_5)(\mu\text{-}C_6F_5Cl)(C_6F_5)_4]$ (**3**) in CH_2Cl_2.

and oxidized species in a reversible one electron process. When an increasing potential (0.90–1.50 V) is applied to a CH_2Cl_2 solution of complex **4**, no reversible oxidation waves are observed (see Figure 8). As already noted, this result is not what might have been anticipated from the theoretical calculation.

Figure 9 shows the cyclic voltammogram of a solution of $(NBu_4)[(C_6F_5)_2Pt(\mu\text{-}C_6F_5Cl)(\mu\text{-}C_6F_5)Pt(C_6F_5)_2]$ (**3**) in CH_2Cl_2 for a scan between +1.200 and –0.090 V vs SCE. The section between +1.200 and +0.550 V (dotted line) indicates the absence of any redox activity for the binuclear complex within this region. On scanning to –0.090 V (0.200 V·s^{-1}), however, we observe an interesting feature. An irreversible reduction wave appears at 0.265 V; and associated with this reduction is the consequent appearance of coupled oxidation and reduction peaks corresponding to the reversible one-electron interconversion of complex **2** and complex **4**. On recycling the scan, we observe that on subsequent cycles the irreversible reduction loses current density and the reversible couple is strengthened. We conclude that as complex **3** is irreversibly reduced (to the dianionic species **2**), further recycling of the voltage diminishes the intensity of this reduction. At the same time, as the concentration of complex **2** grows, the current density of the reversible **2**–**4** one-electron couple increases.

Experimental Section

Infrared spectra, C, H, and N analyses, and conductance measurements were performed as described elsewhere.[1] ^{19}F NMR spectra were recorded on a Varian XL-200 instrument. Negative ion FAB mass spectra were recorded on a VG-Autospec spectrometer operating at ca. 30 kV, using the standard cesium ion FAB gun. 3-Nitrobenzyl alcohol was used as matrix. Cyclic voltammetric measurements were performed on an EG&G PARC Model 273 potentiostat. A three-electrode system was used, which consisted of a platinum disk working electrode, a platinum file auxiliary electrode, and a saturated calomel reference electrode. The measurements were carried out on CH_2Cl_2 solutions with 0.1 M $(NBu_4)PF_6$ as supporting electrolyte.

(a) Reaction of $(NBu_4)[Pt_2(\mu\text{-}C_6F_5)_2(\mu\text{-}AgOEt_2)(C_6F_5)_4]$ (1) with X_2. X = Cl. To a suspension of **1** (0.80 g, 0.44 mmol) in toluene (40 mL) was added a solution of Cl_2 in CCl_4 (5 mL, 3 mmol). The color of the mixture changed to dark garnet. The mixture was stirred at room

temperature for 15 min and was then filtered. The resulting dark garnet solid was treated with CH_2Cl_2 (10 × 15 mL), and the remaining white solid was identified as AgCl. The CH_2Cl_2 solution was evaporated to dryness, and the dark garnet solid, **3**, was washed with toluene (10 mL) and *n*-hexane (5 mL). Yield: 90%. IR data (cm^{-1}): 1700 s, 1650 vs, 1627 s, 1500 vs, 1320 s, 1296 vs, 1258 vs, 1165 vs, 1085 vs, 1076 vs, 1060 vs, 1000 s, 971 vs, 960 vs. X-sensitive modes: 802 vs (sh), 790 vs.

X = I. To a toluene suspension (40 mL) of **1** (0.600 g, 0.330 mmol) was added an excess of I_2 (0.251 g, 0.991 mmol), and the mixture was stirred at room temperature for 1 h. The resulting black solid was filtered and treated with CH_2Cl_2 (15 × 15 mL); and the insoluble (in CH_2Cl_2) residue was identified as AgI. The black CH_2Cl_2 solution was evaporated to dryness, and the resulting black solid was washed with toluene (10 mL) and $CHCl_3$ (5 mL). Yield of **4**: 49%. IR data (cm^{-1}): 1630 m, 1612 m, 1574 m, 1498 vs, 1320 s, 1244 s, 1076 vs, 1060 s, 972 vs, 958 s. X-sensitive modes: 802 s, 792 s, 775 m.

The reaction of **1** with Br_2 was carried out similarly. A 0.200-g (0.105 mmol) sample of compound **1**, 0.6 mmol of Br_2, and 20 mL of toluene were used. Compound **4** was obtained in 41% yield.

(b) Reaction of $(NBu_4)_2[Pt_2(\mu\text{-}C_6F_5)_2(C_6F_5)_4]$ (2) with X_2 (X = Br, I, Cl). X = Br. A sample (0.200 g, 0.105 mmol) of **2** in a toluene/THF (30/5 mL) solution was treated with 0.82 mL (0.32 mmol) of Br_2 in CCl_4; and the mixture was stirred at room temperature for 1 h. The resulting solution was evaporated to dryness, and the oily residue was treated with ^{i}PrOH (10 mL). After 4 h of stirring, the resulting white solid $(NBu_4)_2[Pt_2(\mu\text{-}Br)_2(C_6F_5)_4]$ was separated and identified by IR and C, H, and N analyses.[18] Upon standing at room temperature for 2 days, the mother liquors produced more white solid. Total yield: 60%.

X = I. To a toluene/THF solution (30/5 mL) of **2** (0.400 g, 0.210 mmol) was added I_2 (0.162 g, 0.640 mmol), and the mixture was stirred at room temperature for 1 h. The resulting solution was evaporated to dryness, and the residue was treated with *n*-hexane (4 × 15 mL) and then twice with a mixture of OEt_2 and *n*-hexane (10/40 mL). The resulting dark solid was treated with MeOH (5 mL), yielding a white solid identified (IR and C, H, N, analyses)[1] as $(NBu_4)_2[Pt_2(\mu\text{-}I)_2(C_6F_5)_4]$ (73% yield).

X = Cl. To a CH_2Cl_2 solution (30 mL) of **2** (0.15 g, 0.080 mmol) was added Cl_2 in CCl_4 (1 mL, 0.6 mmol), and the mixture was stirred at room temperature for 10 min and then evaporated to dryness. The residue was treated with toluene, yielding a dark garnet solid, **3**, in 50% yield.

(c) Reaction of $(NBu_4)[Pt_2(\mu\text{-}C_6F_5)_2(C_6F_5)_4]$ (4) with Cl_2. To a CH_2Cl_2 solution (30 mL) of **4** (0.04 g, 0.02 mmol) was added a CCl_4 solution of Cl_2 (0.4 mL, 0.2 mmol), and the mixture was stirred at room temperature for 10 min. The resulting solution was evaporated to dryness, and the residue was treated with toluene (5 mL), yielding compound **3** (50% yield).

(d) Reaction of $(NBu_4)[(C_6F_5)_2Pt(\mu\text{-}C_6F_5)_2Pt(C_6F_5)_2]$ (4) with $(NBu_4)_2[Pt(C_6Cl_5)_4]$. To 30 mL of a CH_2Cl_2 solution of **4** (0.100 g, 0.0612 mmol) was added $(NBu_4)_2[Pt(C_6Cl_5)_4]$ (0.1026 g, 0.0612 mmol), and the mixture was stirred at room temperature for 30 min. The solution was evaporated to dryness, and the residue was treated with $CHCl_3$ (15 mL), yielding a blue solid identified as $(NBu_4)[Pt^{III}(C_6Cl_5)_4]$. After filtration, the resulting solution was evaporated to dryness, and the residue was treated with Et_2O so that more $(NBu_4)[Pt(C_6Cl_5)_4]$ was obtained (total yield 89%). The diethyl ether solution was evaporated to dryness, and the orange residue was washed with ^{i}PrOH (5 mL), yielding a deep yellow solid, compound **2**, in 51% yield.

(e) X-ray Structure Analysis of $(NBu_4)[Pt_2(\mu\text{-}C_6F_5Cl)(\mu\text{-}C_6F_5)(C_6F_5)_4]$ (3). Crystals of complex **3** were obtained by slow diffusion of hexane into a dichloromethane solution of the complex at −30 °C. All attempts to grow suitable crystals for X-ray diffraction rendered only thin needles and fine plates. Using readily available facilities, we gathered data three times, from three crystals varying in thickness from 10 to 15 μm—(1) at 4 °C with a conventional diffractometer; (2) at ambient temperature using a rotating anode; and (3) at −83 °C with a conventional diffractometer and specially controlled diffraction geometry. While all three attempts yielded qualitatively similar results, number (3) gave a data set which we judged superior to the others; this is the determination which we report here.

A fine garnet plate of dimensions 0.489 (bounded by the form ⟨001⟩) × 0.129 (⟨100⟩) × 0.015 (⟨010⟩) mm was mounted at the end of a quartz fiber. The crystal was mounted on end, with the face (001) pressed into a thin layer of stopcock grease at the end of the fiber. As the crystals were exceedingly fragile, we used only a small amount of epoxy at each end of the line of contact between the crystal and the fiber. The sample was transferred to the nitrogen cold stream on the diffractometer and allowed a period of time to equilibrate thermally before the beginning of measurements.

The crystal system, lattice type, Laue group, and cell parameters were determined by routine procedures.[19] The Laue group and lattice parameters were verified by normal-beam oscillation photos taken about [100], [010], [001], and [110]. Geometrical data are summarized in Table II. For intensity data collection, the azimuthal angle ψ was calculated individually for each reflection in such a way as to keep the lattice vector [010] as close as possible to the scattering plane—the so-called "flat mode" of the diffractometer. This technique is intended to minimize to whatever extent possible the effects of absorption. We also used the learned profile method for intensity data collection, expecting that the use of the "flat mode" would attenuate any inaccuracies that mosaic anisotropy might cause in the learned profile. Three monitor reflections, remeasured periodically during the course of data collection, did not reveal any observable crystal decay.

For the application of numerical absorption corrections to the data, we indexed the faces of the crystal and measured its size on a Huber optical goniometer. Since special geometry was used for data collection, the necessary direction cosines were calculated[20] for each datum from its actual experimental geometry, as recorded by the diffractometer in the raw data file. After absorption correction,[21] the merging *R*-factor for 4329 unique data (from 4951 measurements) was 0.0174.

Systematic absences were consistent with the centric group *C*2/*c* or the acentric group *Cc*. In either case, the cell contains four units of $(NBu_4)[Pt_2(\mu\text{-}C_6F_5)(\mu\text{-}C_6F_5Cl)(C_6F_5)_4]$. The structure can be solved in the acentric group, with all moieties lying on general positions, or in the centric group, with the dinuclear anion lying across a center of symmetry and with the NBu_4 cation on a 2-fold axis. As the choice between these two possibilities turned out to be quite ambiguous, we shall describe the resolution of the structure in some detail.

Allowing for practical differences between the use of *Cc* and of *C*2/*c* for this structure, we found the development of the structure to be the same in both groups. The platinum atoms, the terminal C_6F_5 ligands, and the NBu_4 cation were easily located and refined; however, in either group the electron density of the bridging ligands was poorly defined and poorly fitted by traditional atomic models. In the development of the structure in either space group, the meta and para positions of the bridging ligands were particularly difficult to define; furthermore, we could clearly see that there were both in-plane and out-of-plane substituents at the para position of the bridging ligands. (Indeed, it was from this fact that the identity of the complex anion was first inferred.)

We completed the refinement of the structure in two ways—in space group *Cc* and without disorder in the model of the bridging ligands, and in space group *C*2/*c*, with the anion lying across a center of inversion and with the aromatic and nonaromatic bridging ligands disordered across the center. The refinement in space group *Cc* converged poorly in both enantiomorphs. While all atomic sites were located in difference maps, geometrical restraints were necessary for the C_6F_5Cl bridge; and it was necessary to refine the aromatic C_6F_5 bridge as a rigid group. Two facts suggested that this model had merit—(1) that a final difference map showed a paucity of evidence for disorder, and (2) that with geometrical restraints applied to bonded distances only, the nonaromatic bridge took on a semiboat conformation. Nevertheless, more detailed consideration of the resulting model, consisting of a graphical superposition of the bridging ligands and an analysis of the distribution of the phases ϕ_{calc} calculated from the model, indicated quite strongly that the distribution of electron density described by this model was so nearly centric that it would be erroneous to describe the structure as acentric. (More details are available as supplementary material.) We thus used the results of the refinement in *Cc* as a point of departure for the final refinement in the centric group *C*2/*c*.

In space group *C*2/*c*, the asymmetric unit comprises half of one dinuclear anion and half of a tetrabutylammonium cation. The cation and the terminal ligands of the anion refined with no complication. For the bridging ligands, we simply constructed a superposition of the two bridging ligands which had come out of the acentric refinement, using

(18) Usón, R.; Forniés, J.; Martínez, F.; Tomás, M. *J. Chem. Soc., Dalton Trans.* **1980**, 888.

(19) Bino, A.; Cotton, F. A.; Fanwick, P. E. *Inorg. Chem.* **1979**, *18*, 3558.

(20) Falvello, L. R. Xreduce; Fortran program for CAD-4 direction cosines; 1990.

(21) The main body of crystallographic computation was conducted on a Network Interconnect VAXcluster (VMS V5.5) with the program package SHELXTL-PLUS Release 4.21/V: Siemens Analytical X-ray Instruments, Inc., Madison, WI, 1990.

a rigid group for each. Of the atoms of the bridging ligands, only the F and Cl substituents at the para position of the C_6F_5Cl ligand were not included in a rigid group. These two atomic sites were modeled as superpositions of F and Cl atoms, with populations constrained to produce the correct overall stoichiometry. The population parameter refined to nearly half-occupancy for F and Cl at each site. It must be emphasized that our model for the bridging ligands was meant to reproduce the observed electron density as closely as possible, within the bounds of the convolution approximation, the conventional atomic structural model. We do not attribute any chemical significance to the Pt–C_{bridge} distances deduced from this refinement, or to the angles involving the C_{ipso} atoms of the bridging ligands. We do note, however, that all other indicators of the reliability of the refinement are positive. The atoms of the cation behaved well, and the terminal C_6F_5 ligands exhibited the subtle and characteristic reduction in the symmetry of the C_6 ring from D_{6h} to C_{2v}. This effect, which is visible as a diminution of the C–C_{ipso}–C angle to a value well below 120°, and which is caused by the presence of electronegative substituents on the phenyl ring, is an effective measure of the quality of a refinement involving such groups.

Anisotropic displacement parameters were used for all non-hydrogen atoms, including those of the bridging ligands. For the latter, we consider this more an exercise in imaging than an attempt to extract valid atomic parameters, an endeavor rendered impossible by the nature of the crystal. Chemically similar atomic sites and spatially proximal sites in the superposed bridges were tied to the same sets of anisotropic displacement parameters. The terminal C_6F_5 ligands and the non-hydrogen atoms of the tetrabutylammonium cation refined freely. For the methylene moieties of the butyl groups, hydrogen atoms were placed at calculated positions and refined as riders, with a single isotropic displacement parameter applied to all hydrogen atoms.

Three data which were badly reproduced in preliminary refinement, and which we considered to have been poorly measured, were omitted from the refinement. (Several other reflections which were poorly reproduced, but which we could not judge to have been badly measured, were left in.) In the final refinement, then, 353 variable parameters were fitted to 2447 data, for a data-to-parameter ratio of 6.9. We observed, as expected, a modest amount of correlation among the rigid-group rotational and translational parameters of the bridging ligands, and also between displacement parameters of the bridging ligands and the rigid-group parameters. Nevertheless, the refinement converged well, with the residuals given in Table II.

(f) X-ray Structure Analysis of $(NBu_4)[Pt_2(\mu\text{-}C_6F_5)_2(C_6F_5)_4]$ (4). Crystals of complex **4** were obtained by slow evaporation of a concentrated dichloromethane solution of the complex at −30 °C.

Geometric and intensity data were taken from an opaque, pinacoidal crystal which had been mounted at the end of a glass fiber and covered with a thin layer of epoxy cement. Routine CAD-4 data-collection procedures[19] were used in unit-cell and symmetry determination. Axial photographs were used to verify the lattice dimensions and Laue group ($2/m$). Important crystal data are listed in Table II.

Intensity data were reduced by routine procedures.[22] Data reduction included corrections for absorption[23] (based on azimuthal scans of reflections with Eulerian angle χ near 90°) and for decay—since the intensities of two monitor reflections dropped by an average of 10.6% over the course of 90 h of X-ray exposure time.

The location of the unique platinum atom was derived from a Patterson map, and the remainder of the structure (excluding hydrogen atoms) was developed and refined[21] in an alternating sequence of least-squares cycles and difference Fourier maps. The final refinement included anisotropic displacement parameters for all non-hydrogen atoms. Hydrogen atoms of the CH_2 entities of the tetrabutylammonium cation were added at calculated positions and treated as riding atoms, with a single common isotropic displacement parameter for all of them. Relevant parameters and residuals from the refinement are given in Table II. The data-to-parameter ratio was 6.6:1. We observed no significant correlation coefficients from the final refinement; and listings of the residuals as functions of $\sin\theta/\lambda$, $|F_{obs}|$, h, k, l, and parity group showed no systematic trends in the least-squares variance.

Acknowledgment. We thank Dr. Jesus Orduna for the mass spectrum of compound **3**. We thank Prof. R. Alcalá (Zaragoza) for EPR measurements and Dr. G. Garcia-Herbosa (Burgos) for preliminary electrochemical measurements. Financial support from the Comisión Interministerial de Ciencia y Tecnología (Spain) (Project PB91-0692) and the U.S. National Science Foundation is gratefully acknowledged.

Supplementary Material Available: Listing of atomic coordinates, full tables of bond distances and bond angles, anisotropic displacement parameters, and graphical information about the acentric refinement for **3**, plots of observed and calculated mass spectra in the region of the negative ion peak for **3**, and listings of atomic coordinates, bond distances, bond angles, and anisotropic displacement parameters for **4** (24 pages); listing of structure factors for **3** and **4** (29 pages). Ordering information is given on any current masthead page.

(22) For the structure of compound **4**, data reduction and preliminary crystallographic calculations were done by a VAX-11/780 (VMS V4.4) with programs from the package SDP/VAX V3.0.

(23) North, A. C. T.; Phillips, D. C.; Mathews, F. S. *Acta Crystallogr., Sect. A: Cryst. Phys. Diffr., Theor. Gen. Crystallogr.* **1968**, *24*, 351.